

Effect of Lanthanum Content on the Formation of Acicular Ferrite



YUMIN XIE, MINGMING SONG, HANGYU ZHU, JIANLI LI, GUOJUN MA,
and ZHENGLIANG XUE

The microstructure and inclusions in the heat-affected zone (HAZ) of steel with two different contents of rare earth (RE) lanthanum (La) were investigated. The results indicated that when the content of La was 0.010 wt pct in steel, the area percent of acicular ferrite (AF) was 62.9 pct and the main composition of inclusions was La–O–S–Ti–Mg + MnS, whereas in steel with 0.068 wt pct La, the area percent of AF decreased to 36.9 pct and the main composition of inclusions changed to La–O–P + La–P. Both the mean size and the number of inclusions in the steel with high content of La were larger than those in the steel with low content of La. The ratios of effective inclusions, which can act as the nucleus of AF in the two steels, were 59.2 and 36.5 pct, respectively. In the two steels, the size of effective inclusions was concentrated in 1 to 4 μm . Although the main effective inclusions in the two steels were both RE inclusions, in the steel with low RE content, the effective RE inclusions were mainly composites of La–O–S–Ti–Mg and MnS, while in the steel with high RE content, these effective RE inclusions were La–O–P and La–O–P + TiN. The effective inclusions in low RE content steel were more capable than those in high RE content steel, and the mean numbers of AF laths induced by effective inclusions in the two steels were 2.9 and 2.3, respectively.

<https://doi.org/10.1007/s11663-022-02458-w>

© The Minerals, Metals & Materials Society and ASM International 2022

I. INTRODUCTION

ACICULAR ferrite (AF) is a kind of chaotic interlocking microstructure formed on the surface of inclusions within the grain of austenite.^[1–3] When the content of AF increases from 7.2 to 34.8 pct, the low-temperature impact toughness at 253 K ($-20\text{ }^\circ\text{C}$) can increase by 3 times in the heat-affected zone (HAZ) of the X70 pipeline steel.^[4] Generally, the formation of AF is affected by the type, size, and number of inclusions.^[5,6] Byun *et al.* found that in non-Al-killed steel with 1.60 wt pct Mn, the typical inclusions changed from Mn–Ti–O to Ti_2O_3 when Ti increased from 0.0045 to 0.0110 wt pct and Ti_2O_3 could induce the formation of a large amount of AF.^[7] Shim *et al.* further indicated that pure Ti_2O_3 could not induce the nucleation of AF in no-Mn steel, while Ti_2O_3 would be transformed into

$(\text{Ti, Mn})_2\text{O}_3$ in Mn-containing steel, which could strongly induce the nucleation of AF.^[8] Song *et al.* found that the size of inclusion that was beneficial to the nucleation of AF mainly concentrated in the range 1 to 4 μm .^[9] Furthermore, Lee *et al.* pointed out that within the size range favorable for the nucleation of AF, the larger inclusion was more preferable for the nucleation of AF.^[10] Kim *et al.* said that the amount of AF was proportional to the number of inclusions smaller than 2 μm .^[11]

During the process of the welding thermal cycle in the HAZ, microstructure is prone to coarsening easily. A large amount of side-plate-like ferrite, such as Widmanstätten ferrite and upper bainite, formed during the cooling process, which leads to great deterioration to the properties of steel.^[7,12] When a proper amount of Ti was added into the steel, TiN and Ti_xO_y were produced. Both TiN and Ti_xO_y can significantly improve the microstructure in the HAZ. TiN pins the grain boundary to inhibit the coarsening of austenite grain. Ti_xO_y induces the nucleation of AF to refine the microstructure of steel. However, the thermal stability of TiN is poor. With the increase of welding heat input, TiN disappears easily during the thermal cycle process, which leads to a sharp decrease in the number of TiN, and then the role of grain boundary pinning is weakened. Moreover, the deoxidation ability of Ti is not very strong in steel, and the production of a large

YUMIN XIE, MINGMING SONG, HANGYU ZHU, JIANLI LI, GUOJUN MA, and ZHENGLIANG XUE are with the The State Key Laboratory of Refractories and Metallurgy, Wuhan University of Science and Technology, Wuhan 430081, P.R. China and the Key Laboratory for Ferrous Metallurgy and Resources Utilization of Ministry of Education, Wuhan University of Science and Technology, Wuhan 430081, P.R. China. Contact e-mail: smma987@163.com; zhuhy@wust.edu.cn

Manuscript submitted October 25, 2021; accepted January 23, 2022.

Article published online February 20, 2022.

number of Ti_xO_y requires high oxygen content. Obviously, this is impractical in high clean steel. It is hard for Ti treatment to achieve the desired effect of refining microstructure in the HAZ.^[13] For Mg treatment, a lot of MgO, whose thermal stability is great, can form after Mg is added into steel. It is well known that although MgO has low ability to induce the nucleation of AF, it can pin the grain boundary effectively in steel.^[14] Song *et al.* compared the Ti–Mg treated steel with Ti treated steel and found that the grain size of austenite was smaller and the impact toughness was higher in the HAZ of Ti–Mg treated steel.^[15] However, during the actual producing process, the content of Mg is difficult to control. Besides that, when Mg is added into Ti-containing high clean steel, Ti_xO_y would be hard to form as the deoxidization ability of Mg is stronger than that of Ti.^[16] The AF nucleus cannot form easily when Ti and Mg are added to the composite. It is clear that the deoxidization and desulfurization ability of rare earth (RE) is slightly stronger than that of Mg in steel, and RE inclusions can induce the nucleation of AF effectively, which can refine the microstructure in the HAZ.^[17–21] When RE is composited with Ti–Mg, RE can make up for the lack of AF nucleus by forming a large amount of RE inclusions in steel. More and more researchers have become interested in Ti–Mg–RE composite treatment. Liu *et al.* found that the main type of inclusion in Ti–Mg deoxidized steel was MgO–Al₂O₃–MnS. After 0.014, 0.024, and 0.037 wt pct Ce was added, inclusions became CeAlO₃–MgO–MnS, Ce₂O₃S–MgO–MnS, and Ce₂O₂S–MnS, correspondingly.^[22] Ce-containing inclusion can refine the microstructure by promoting the formation of AF. Wang *et al.* concluded that there were a lot of inclusions composited of Ti–Mg–Ce–O in V-containing steel treated by Ti–Mg–Ce.^[5] V-containing precipitate could enhance the nucleation of AF on Ti–Mg–Ce–O inclusions. Thus far, the influence of RE content on the composition/size of the nucleus in Ti–Mg–RE composite treated steel is still unclear. Ti–Mg–RE–O composite inclusions often contain many different composition parts.^[23] The influences of the inclusion structure on the nucleation of AF are also unknown. In the present work, the differences between microstructure and inclusion were compared in Ti–Mg–RE (La) treated steel with two different contents of lanthanum. The effectiveness of different inclusions in inducing the nucleation of AF was explored, and the action mechanism of inclusions was analyzed.

II. MATERIALS AND METHODS

A. Material

Two steels with 0.010 and 0.068 wt pct La were smelted in a vacuum high-frequency induction furnace. Depending on the content of La, two steels were named as steel L (for low La) and steel H (for high La). The compositions are shown in Table I. After melting, the solid ingots (about 60 kg) were soaked at 1373 K (1100 °C) for 2 hours to homogenize the composition. Then, the ingots were forged into steel blocks with a cross section of 130 × 80 mm². The forging temperature of the ingots was 1373 K to 1123 K (1100 °C to 850 °C). Then, the steel blocks were rolled into plates after being reheated to 1373 K (1100 °C). The rolling temperature was controlled in 1373 K to 1123 K (1100 °C to 850 °C) as well. After hot rolling, the plates were air cooled to room temperature. The final thickness and width of the plate were 15 and 250 mm, correspondingly.

B. Methods

Specimens for welding simulation with the dimensions of 11 × 11 × 70 mm³ were obtained from the steel plates at the center of the thickness and one-quarter of the width. The longest side of each specimen was parallel to the width of the steel plate. After specimen polishing, the welding simulation test was carried out by a Gleeble 3800 testing machine. During the thermal cycle modeling process, the specimen was heated to 1623 K (1350 °C) at a rate of 100 K/s (100 °C/s). Then, it was held at this temperature for 1 second. After that, the specimen was cooled to room temperature and the cooling time from 1073 K to 773 K (800 °C to 500 °C) ($\Delta t_{8/5}$) was 400 seconds. Four tests were repeated for the thermal simulation in each steel. The sample preparation and thermocouple position are shown in Figure 1.

One thermal simulation specimen of each steel was cut from the welding spot and then polished to obtain a metallographic specimen. A scanning electron microscope (SEM, EVO 010, Zeiss) with energy dispersive spectrometry (X-Max^N 79416, Oxford) was used to observe the inclusion in the HAZ. A nonrepetitive test area of about 1.17 mm² was taken randomly on the test surface of the specimen in each steel. The size and number of the inclusions in the test area were counted. The size of inclusions was estimated by the equivalent circle diameter. Finely polished metallographic specimens were etched chemically using a solution of 3 pct

Table I. Composition of the Experimental Steel Samples (Mass Percent)

Sample	C	Si	Mn	P	S	O	La	Mg	Ti	N	Fe
Steel L	0.16	0.30	1.38	0.027	0.0048	0.0032	0.010	0.0006	0.0046	0.0025	bal.
Steel H	0.16	0.31	1.38	0.027	0.0012	0.0012	0.068	0.0010	0.0180	0.0026	bal.

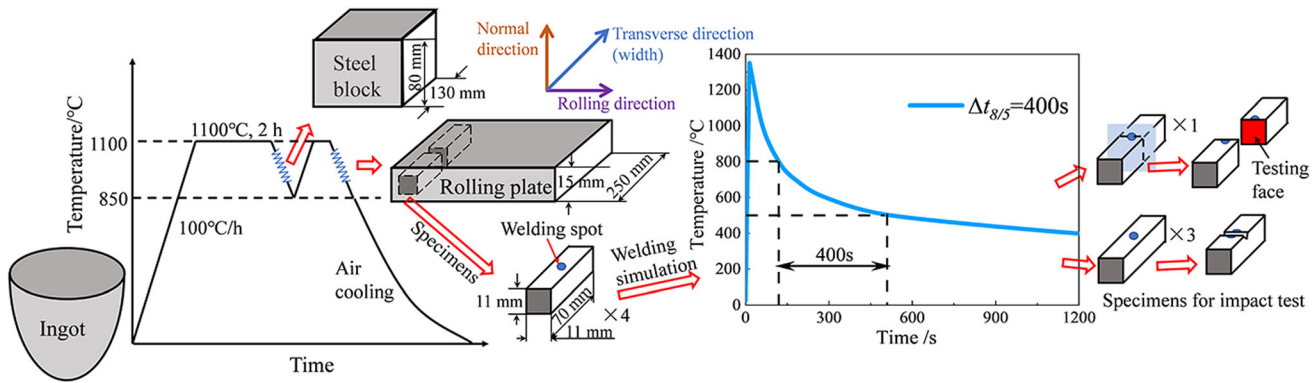


Fig. 1—Schematics of manufacturing process and welding simulation process.

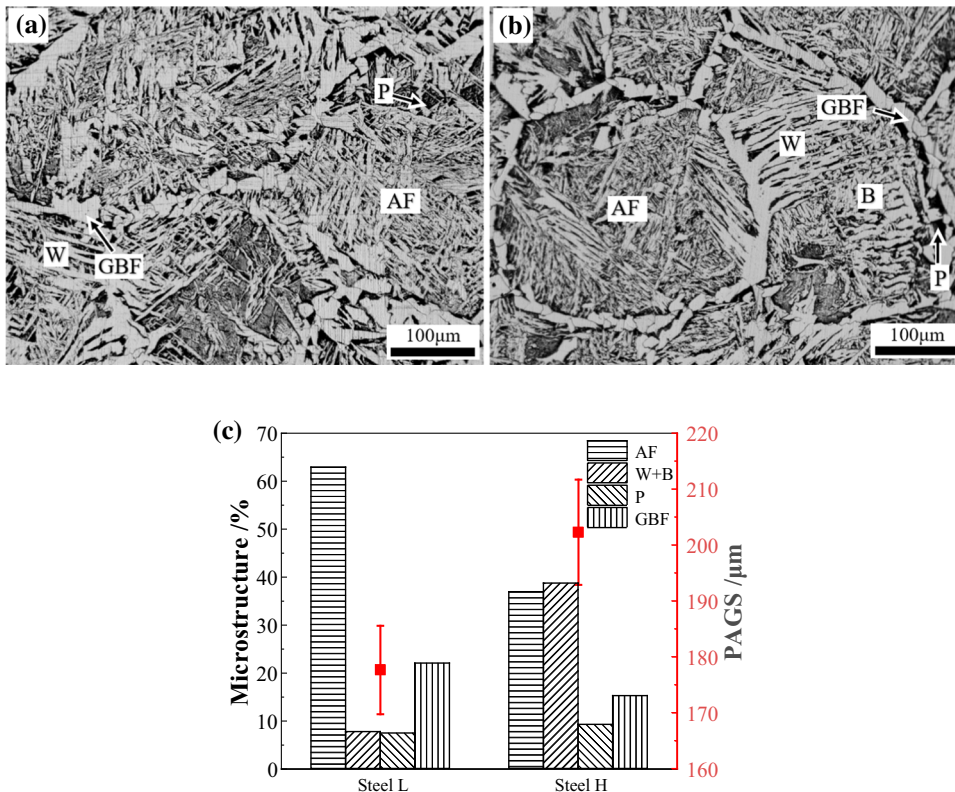


Fig. 2—Morphology of microstructure in HAZ in (a) steel L and (b) steel H; (c) microstructure statistical result.

nitric acid in ethanol. After that, the microstructure in the HAZ was observed with an optical microscope (6XB-PC, Shang Guang). The intercept method was used to characterize the prior austenite grain size (PAGS) in each specimen. More than 10 pictures were processed to obtain the size of the PAGS. The mean value was taken as the experimental result, and the standard deviation was considered as the experimental error. Different microstructures were identified and painted with different colors; then, Image J software was used to individually obtain the area percent of the corresponding microstructures.

The remaining three thermal simulation specimens of each steel were machined into standard Charpy “V” notch samples with dimensions of $10 \times 10 \times 55 \text{ mm}^3$. Before the impact test, the impact specimens were kept at 253 K (-20°C) for 20 minutes. The impact test was carried out on a drop weight impact tester. The mean value of three tests was taken as the experimental result, and the standard deviation was the experimental error. An ultradepth three-dimensional microscope (VHX-5000, Keyence) and SEM were used to perform morphological analysis of fracture.

III. RESULTS

A. Microstructure in HAZ

The morphology and statistical results of the microstructure in the HAZ of the two steels are shown in Figure 2. As shown in Figures 2(a) and (b), there was little difference in the types of microstructure between the two steels. There was clear grain boundary ferrite (GBF) along the grain boundary of prior austenite, some side-plate-like Widmanstätten (W) and bainite (B), some AF, and a small amount of pearlite (P) in both steels. The statistical results of the microstructure and PAGS in Figure 2(c) show that the content of AF was 62.9 pct in steel L, while the content of AF was significantly reduced to only 36.9 pct in steel H. Compared with steel L, W + B was obviously increased in steel H. Both the morphology and statistical results of the microstructure in the two steels showed that more AF was formed in the HAZ of steel L, while more W + B was found in steel H. Besides that, the prior austenite grain of steel H coarsened obviously and the PAGS of steels L and H were 177.7 and 202.3 μm , respectively.

B. Inclusions

Figure 3 shows the morphology of typical inclusions in the two steels. It can be seen from Figures 3(a) and (b) that the main inclusion in steel L was the inclusion composite of La–O–S–Ti–Mg and MnS. The size of this composite inclusion was about 4 μm . The content of La–O–S was dominant in the La–O–S–Ti–Mg composite inclusion, and the contents of Ti and Mg were very low. MnS could precipitate on the surface of La–O–S–Ti–Mg and in the steel matrix randomly. The typical inclusions in steel H are shown in Figures 3(c) through (f). The main inclusions were La–P and La–O–P, and there was a small amount of composite inclusion La–O–P + TiN in steel H. Furthermore, there were a few La–O–S and TiN. The inclusions in steel H were

quite different from those in steel L. The sizes of La–P and La–O–P were both about 4 μm , while the sizes of La–O–S and TiN were about 2 μm .

The statistical results of the number and size of inclusions in the two steels are shown in Figure 4. In steel L, the number of inclusions was 394.9 mm^{-2} and the mean size of inclusion was 1.3 μm , while in steel H, the number of inclusions increased to 665.9 mm^{-2} and the mean size of inclusions increased to 1.3 μm . In each size range of inclusion, the number of inclusions in steel L was less than that in steel H. Further analysis found that the percentage of inclusions with a size of < 1 μm in steel L was higher than that in steel H, while the percentage of inclusions size of 1 to 4 μm in steel L was lower than that in steel H.

Besides the morphology, composition, size, and number of inclusions, the position distribution is also one of the important features of inclusion. Figure 5 shows the distribution of inclusion in the two steels, in which the abscissa and ordinate represent the X-axis and Y-axis directions of the SEM shoot area, respectively, and the entire plane represents the shoot area. The ruler refers to the different numbers of inclusions corresponding to different color areas. The closer the color is to red, the greater the inclusions, while the closer the color is to blue, the fewer the inclusions. Figure 5 shows the number of inclusions in each area of steel L and steel H. It is clear that the number of inclusions in steel L was lower than that of steel H.

A large number of adjacent and nonrepetitive pictures taken by an SEM were used to count the inclusions. N_i is the number of inclusions in each picture, and \bar{N} is the mean number of N_i . The degree of homogeneity in inclusion dispersion, H , is defined as the reciprocal of the relative standard deviation of \bar{N} :

$$H = \frac{\bar{N}}{\sqrt{\frac{\sum_{i=1}^n (N_i - \bar{N})^2}{n-1}}} \quad [1]$$

where n is the number of pictures.

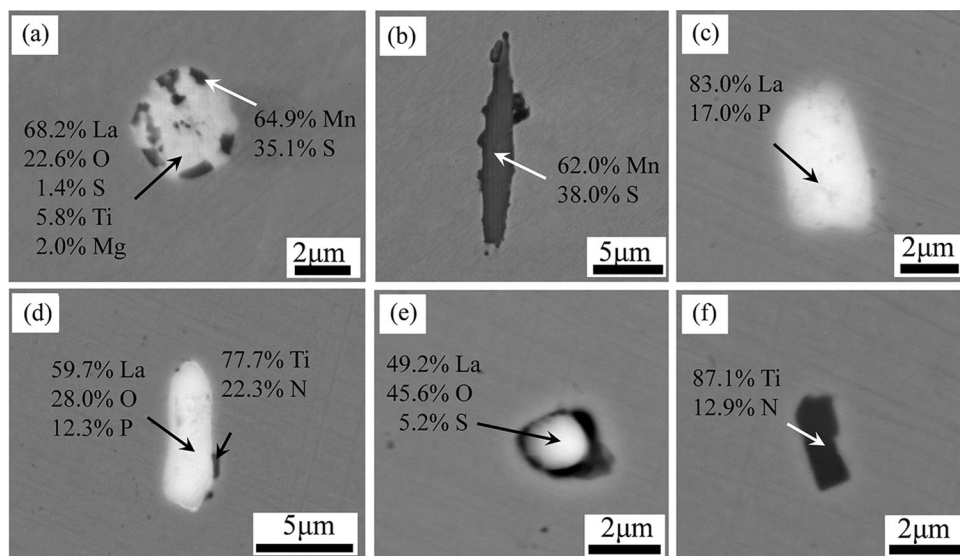


Fig. 3—Typical inclusions in (a) and (b) steel L and (c) through (f) steel H.

The greater the value of H , the greater the homogeneity of the distribution of inclusions. On the contrary, the distribution of inclusions is more concentrated. According to Eq. [1], the values of H in steel L and steel H were 3.9 and 3.2, correspondingly. This means that when the content of La was low, the inclusions in steel were not only less in number but also higher in homogeneity.

C. Low-Temperature Impact Toughness in the HAZ

The impact energies at 253 K ($-20\text{ }^{\circ}\text{C}$) of the two steels are shown in Figure 6. The impact energy in the HAZ of steel L was 56 J, while that of steel H was only 9.1 J. The low-temperature impact energy in the HAZ of steel with low content of La was almost 6 times that of steel with high content of La.

IV. DISCUSSION

A. Composition of the Effective Inclusion

The inclusion that can induce the nucleation of AF is usually called effective inclusion, while the others are referred to as inert inclusion. Figure 7 shows the nucleation of AF induced by the typical effective

inclusion in the two steels. The effective inclusion in steel L was the inclusion composited by La–O–S–Ti–Mg and MnS, as shown in Figures 7(a) through (d). A very small amount of effective inclusion in steel L consisted of La–O + La–O–S, as shown in Figure 7(e). In addition, some Ti_xO_y + MnS could also induce the nucleation of AF in steel L, as shown in Figure 7(f). In steel H, there were two kinds of effective inclusions. The main kind contained La. The composition was La–O–P + TiN and La–O–P, as shown in Figures 7(g) and (h). The second kind had no RE and was mainly TiN, as shown in Figure 7(i).

B. Statistics of AF Nucleation Induced by Inclusions

The number of effective and inert inclusions was counted and the result is shown in Table II. There was little difference in the number of effective inclusions between the two steels, which were 233.8 and 243.1 mm^{-2} , respectively. However, the number of inert inclusions varied greatly—161.1 and 422.8 mm^{-2} , correspondingly. As a result, the percentage of effective inclusion in steel L was about 59.2 pct, which was significantly higher than that in steel H, which was only about 36.5 pct.

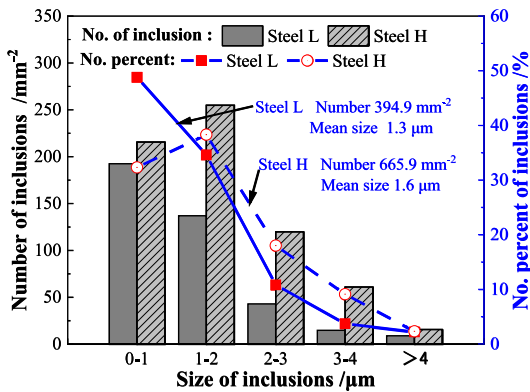


Fig. 4—Size distribution of inclusions in the two steels.

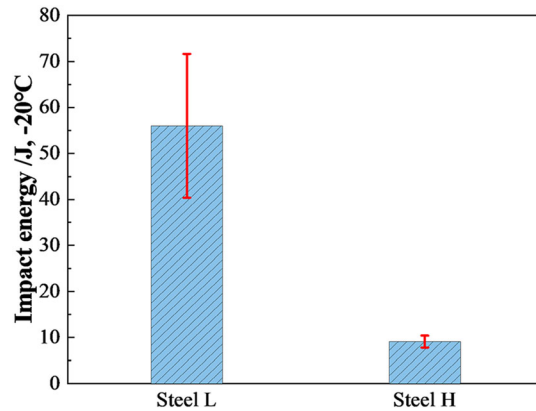


Fig. 6—Impact energy at $-20\text{ }^{\circ}\text{C}$ of the two steels.

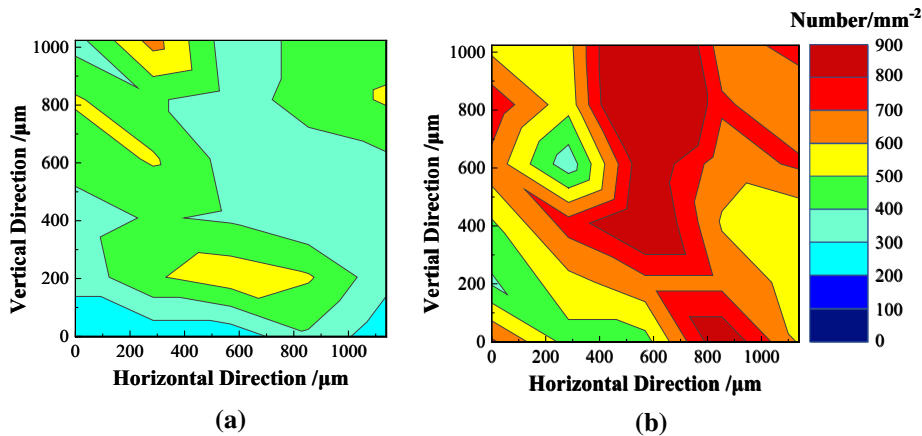


Fig. 5—Number distribution of inclusions in (a) steel L and (b) steel H.

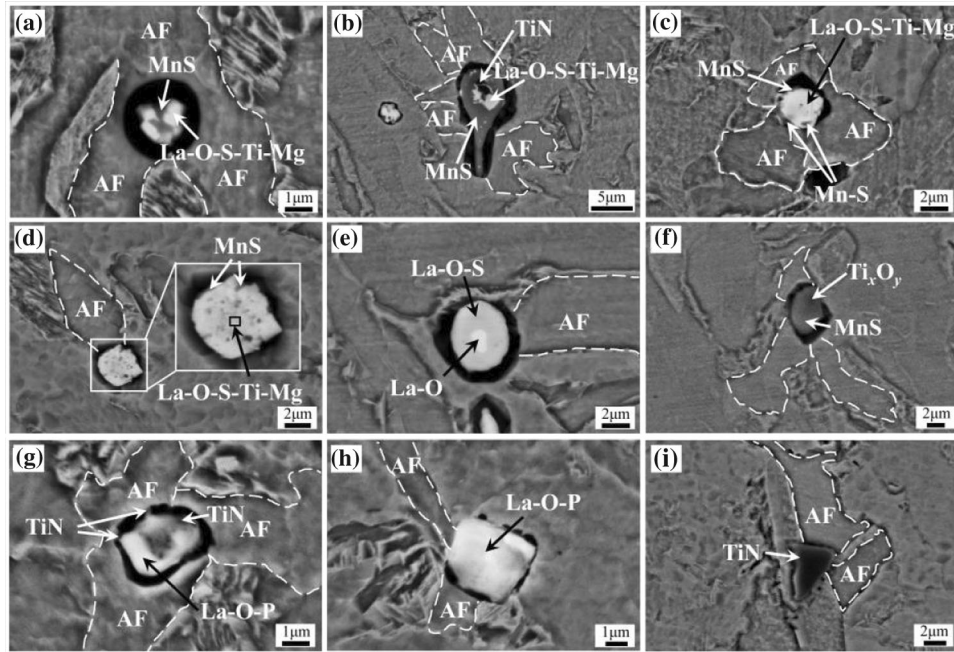


Fig. 7—Typical inclusions inducing the nucleation of AF in (a) through (f) steel L and (g) through (i) steel H.

Table II. Number Statistical Results of Effective Inclusion and Inert Inclusion (mm^{-2})

Sample	Effective Inclusion	Inert Inclusion
Steel L	233.8	161.1
Steel H	243.1	422.8

Figure 7 shows that the effective inclusions for AF nucleation included RE inclusions and no-RE inclusions. It was well known that there were two kinds of contrast for the inclusion morphology in RE treated steel under SEM backscatter^[24]: contrast brighter than the steel matrix and contrast darker than the steel matrix. The brighter part contained RE, while there was no RE in the darker part. RE inclusions were those with a total or parts of a bright region in one inclusion, and the no-RE inclusion had only pure dark contrast. According to this, the influence of RE inclusion on the nucleation of AF was analyzed. The number of inclusions was counted, and the results are shown in Table III. The number of RE inclusions was 230.7 mm^{-2} , which accounted for 58.4 pct of all inclusions in steel L. In steel H, the number of RE inclusions was significantly higher, about 456.2 mm^{-2} , accounting for 68.5 pct of all inclusions. There was little difference in the number of effective RE inclusions between the two steels, which were 181.3 and 189.8 mm^{-2} , accounting for 78.6 and 41.6 pct of RE inclusions in the two steels, respectively. The number of effective no-RE inclusions was correspondingly 52.5 and 53.3 mm^{-2} , which accounted for 32 and 25.4 pct of no-RE inclusion in the two steels, respectively. Comparing the results in Tables II and III shows that the percentages of effective

RE inclusions in the total effective inclusions were 77.5 and 78.1 pct in the two steels, respectively, indicating that the effective inclusion was mainly effective RE inclusion in both steels.

The percentages of the RE and effective inclusions in different size ranges in the two steels were further counted, and the results are shown in Figure 8. There were a few inclusions with a size $> 4 \mu\text{m}$, and the sizes of RE and effective inclusions were mainly concentrated in 1 to $4 \mu\text{m}$ in the two steels. In addition, the size distribution of effective inclusions was similar to that of the RE inclusions in the two steels. That is, the effective inclusion was mainly RE, which was consistent with the analysis results in Table III. Moreover, the percentage of effective inclusions in the RE inclusion for steel L was higher than that for steel H, which made the size distribution of RE inclusions conform to the effective inclusion better in steel L.

Generally, the higher the percentage of effective inclusion, the higher the effectiveness of the inclusion. In order to specifically analyze the influence of RE content on a nucleus's ability to induce the nucleation of AF, the RE inclusions were further classified into two types. Type I was pure RE inclusion with only bright contrast, while type II was composite RE inclusion with multiple contrasts, in which there were at least one bright region and one dark region within one composite inclusion. The nucleation of AF induced by two types of RE inclusions was analyzed, and the results are shown in Table IV. The total numbers of type I and type II inclusions in steel L were 33.2 and 197.5 mm^{-2} , respectively. RE inclusions in steel L were mainly type II, which accounted for 85.6 pct of RE inclusions. The numbers of type I and type II inclusions in steel H were 346.3 and 109.9 mm^{-2} , correspondingly. Contrary to steel L, the RE inclusions in steel H were mainly type I,

Table III. Number Statistical Results of Different Kinds of Inclusions (mm^{-2})

Sample	Total RE Inclusion	Effective RE Inclusion	Inert RE Inclusion	Total No-RE Inclusion	Effective No-RE Inclusion	Inert No-RE Inclusion
Steel L	230.7	181.3	49.4	164.2	52.5	111.7
Steel H	456.2	189.8	266.4	209.7	53.3	156.4

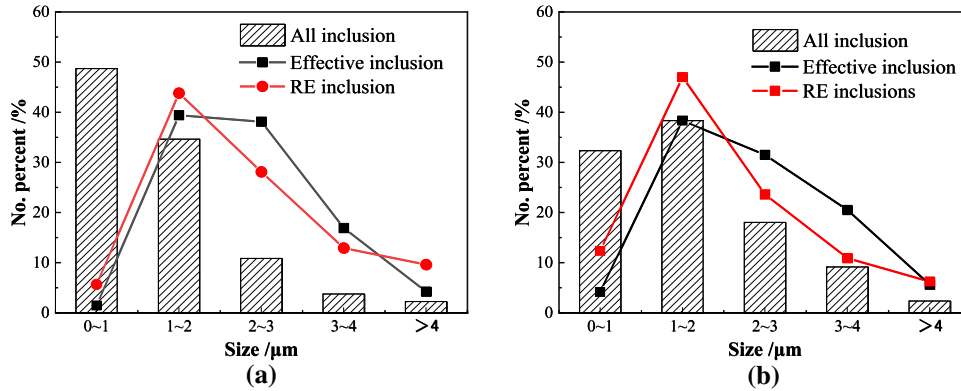


Fig. 8—Size distribution of inclusions in (a) steel L and (b) steel H.

Table IV. Number Statistical Results of Different Types of RE Inclusions

Sample	Type	Total No. (mm^{-2})	Effective Inclusion (mm^{-2})	Percent (Pct)
Steel L	I	33.2	9.9	29.9
	II	197.5	171.4	86.8
Steel H	I	346.3	113.2	32.7
	II	109.9	76.6	69.7

and type II only accounted for 24.1 pct of RE inclusions. Further, the percentages of effective inclusions in type I and type II were quite different. In steel L, the numbers of effective type I and type II inclusions were 9.9 and 171.4 mm^{-2} . Obviously, effective RE inclusion was mainly type II, and the percentage of effective inclusions of type II was 86.8 pct, while in steel H, the numbers of effective type I and type II inclusions were 113.2 and 76.6 mm^{-2} , respectively. The difference between the number of effective type I and type II inclusions was not substantial. In steel H, the percentages of effective inclusions in type I and type II were 32.7 and 69.7 pct, respectively. In both steels, the percentage of effective inclusions in type II was higher than that in type I and the effectiveness of La-O-S-Ti-Mg + MnS in steel L was higher than that of La-O-P + TiN in steel H.

The more AF laths formed on the inclusion, the more effective the inclusion in inducing the nucleation of AF. To further investigate the ability of effective inclusions to induce the nucleation of AF, the effective inclusions observed by SEM were divided into three kinds, as shown in Figure 9. The first was a low-efficiency inclusion with only one AF lath, the second was a medium-efficiency inclusion with two or three AF laths, and the last was a high-efficiency inclusion with four or more AF laths.

In order to facilitate the discussion, the no-RE inclusion was defined as type III. The number of AF laths that nucleated on the type I, type II, and type III inclusions was counted, and the results are shown in Figure 10. Figure 10(a) shows that the effective type II inclusions have the strong ability to induce the nucleation of AF. Most of the effective type II inclusions were medium- and high-efficiency inclusions in steel L, and the mean number of AF laths was 3.1. The ability to induce the nucleation of AF by effective type I and type III inclusions in steel L was lower than that of effective type II inclusions, and the mean numbers of AF laths were 2.7 and 2.6, correspondingly. As shown in Figure 10(b), effective type I, type II, and type III inclusions in steel H were mostly low- and medium-efficiency inclusions and the mean numbers of AF laths were 2.2, 2.4, and 2.1, respectively, which were lower than those of steel L, correspondingly. The mean number of AF laths induced by all effective inclusions in steel L was 2.9, while that of steel H was only 2.3. Figure 10(c) shows that the percentage of medium-efficiency inclusions was the largest in both steels. The percentages of low- and medium-efficiency inclusions in steel L were lower than those in steel H, while the percentage of high-efficiency inclusions was significantly higher than that in steel H. The statistical results showed that

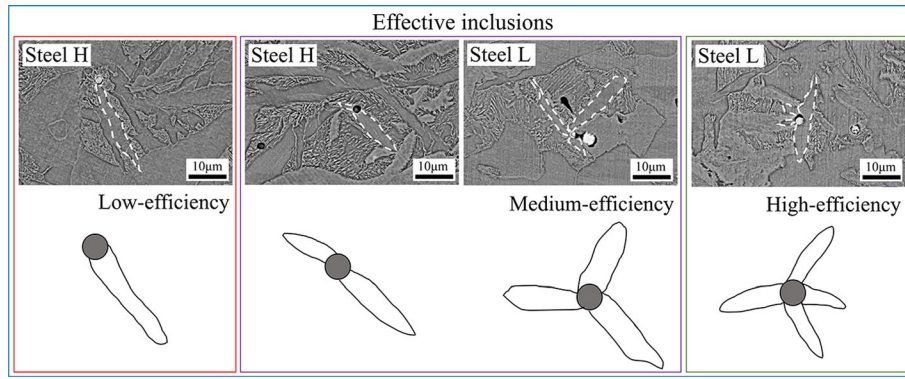


Fig. 9—Schematic diagram of classification of effective inclusions.

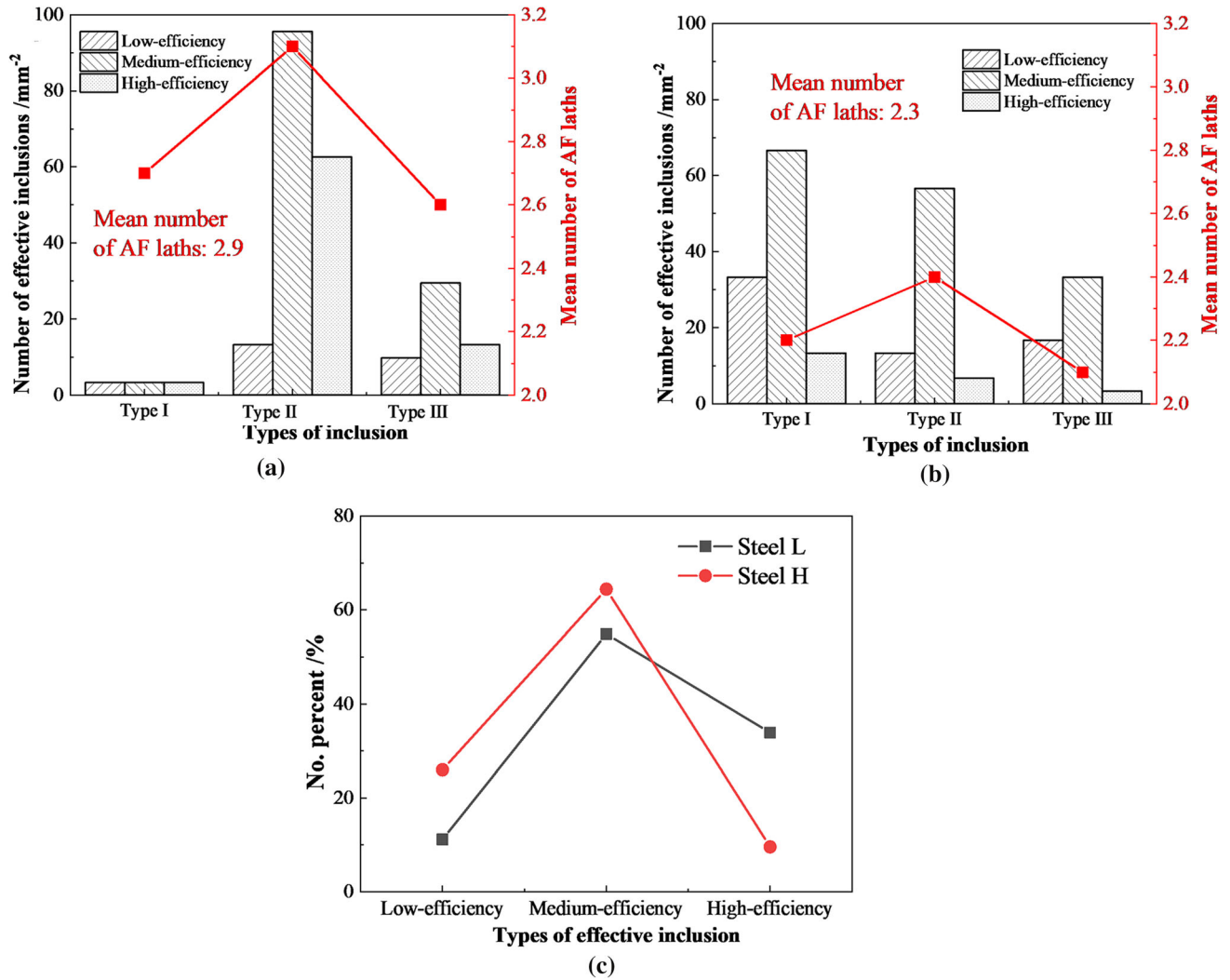


Fig. 10—Statistics of effective inclusion types of (a) steel L and (b) steel H; (c) percentage of effective inclusions in each type.

although there was little difference in the total number of effective inclusions between the two steels, the effective inclusion was mostly a high-efficiency inclusion in steel L, and the mean number of AF laths in steel L was larger than that in steel H, which resulted in more AF in steel L.

C. Mechanism of AF Nucleation on Inclusions

Unfortunately, the mechanism of AF nucleation is still unclear. To date, there are mainly four mechanisms in the academic literature: (1) reducing the interfacial energy between inclusions and AF^[25]; (2) reducing the

Table V. Misfit Between Possible Compounds and α -Fe

Inclusions	Lattice Structure	Lattice Parameters, a (nm)	$a/a_{\alpha\text{-Fe}}$	2-D Misfit (Pct)
La ₂ O ₂ S	hcp	$a = 0.4051$ $b = 0.6943$	1.413	0.2
La ₂ O ₃	hexagonal	0.3943	1.416	2.8
La ₂ S ₃	cubic	0.8616	3.006	0.2
LaP	cubic	0.6025	2.102	4.9
TiN	cubic	0.4238	1.479	3.9
MnS	cubic	0.5230	1.825	8.8
MgO	cubic	0.4110	1.437	5.0

lattice misfit between inclusions and AF to ensure their low interfacial energy^[26]; (3) increasing the elastic strain energy of the matrix around inclusions, arising from the difference in thermal expansion coefficients between inclusions and the matrix^[27]; and (4) increasing the chemical driving force by local Mn depleted in the matrix near inclusions.^[28] It is generally believed that there might be multiple mechanisms at the same time. In different systems, the types of effective inclusions are different and the mechanisms of AF nucleation are also different. Therefore, it is extremely important to further analyze the mechanisms of AF nucleation induced by the inclusions in the two steels.

As shown in Figures 3 and 7, the inclusions in steel L were mainly La–O–S–Ti–Mg + MnS and La–O–S, while they were La–O–P, La–P, TiN, and La–O–P + TiN in steel H. Considering the simple compound compositions of these inclusions, they might be La₂O₂S, La₂O₃, La₂S₃, LaP, TiN, MnS, and MgO.^[29] The two-dimensional (2-D) lattice misfit (δ) between these compounds and α -Fe at the transformation temperature of austenite to ferrite [about 1185K (912 °C)] was calculated as Eq. [2]:

$$\delta_{(hkl)_s}^{(hkl)_n} = \sum_{i=1}^3 \left(\frac{|d_{[uvw]_n}^i - d_{[uvw]_s}^i \cos \theta|}{3 \times d_{[uvw]_n}^i} \right) \times 100\% \quad [2]$$

where $(hkl)_s$ and $(hkl)_n$ are the low index planes of the substrate/particle and nucleated solid/matrix, respectively; $[uvw]_s$ and $[uvw]_n$ are the low index directions in $(hkl)_s$ and $(hkl)_n$, respectively; $d_{[uvw]_s}$ and $d_{[uvw]_n}$ are the interatomic spacings along the $[uvw]_s$ and $[uvw]_n$, respectively; and θ is the angle between $[uvw]_s$ and $[uvw]_n$.

The δ values between these compounds and α -Fe are given in Table V. Bramfitt^[26] found that during heterogeneous nucleation, the smaller the value of δ , the stronger the ability of the compound to induce the nucleation of AF.^[30,31] Among the compounds, the δ values between La₂O₂S/La₂S₃ and α -Fe were the lowest; La₂O₃ and TiN, LaP, and MgO were relatively higher; and MnS was the highest. In steel L, the simple compounds were mainly La₂O₂S, La₂S₃, and La₂O₃, whose δ values were all relatively low. Although the δ values of MgO and MnS were higher than other compounds, their content was very low in steel L. In steel H, the mainly simple compounds contained La₂O₃,

LaP, and TiN, whose δ values were higher than those of La₂O₂S and La₂S₃ in steel L. From the perspective of 2-D lattice misfit theory, the effectiveness to induce AF nucleation of La–O–S–Ti–Mg and La–O–S in steel L was higher than those of La–O–P, TiN, and La–O–P + TiN in steel H.

As is well known, the deoxidation and desulfurization ability of La is stronger than that of Mn. When the content of La in steel was insufficient for complete deoxidation and desulfurization, Mn would play a role in deoxidation and desulfurization. Among the products of deoxidation and desulfurization by La in steel, the $[La]/[O + S]$ of RE inclusions included La₂O₂S, La₂O₃, and La₂S₃ of two-thirds, less than one. According to the combination of La and O + S, the calculation results showed that $3n_{[La]}/2n_{[O+S]}$ in steel L was 0.3, while $3n_{[La]}/2n_{[O+S]}$ in steel H was 6.6. This meant that the content of La in steel L could not be the cause of complete deoxidation and desulfurization. Therefore, Mn had the opportunity to combine with the remaining S, forming MnS. According to the research results of Tomita *et al.*, MnS tends to precipitate on the surface of other inclusions and the Mn-depleted zone is easily formed in the surrounding inclusions, which is beneficial to the formation of AF.^[32] Contrary to steel L, after complete deoxidation and desulfurization, the content of La was still very high in steel H. Then, the remaining La could combine with P, resulting in a large amount of La–O–P and La–P. MnS could not form in steel H. In addition, Ti was in the form of TiN and there was no Ti_xO_y in steel H.

D. Performance and Fracture

Figure 11 shows the impact fracture surface of the HAZs of the two steels. The area percents of ductile zone in the fracture of the two steels were measured at 18.1 and 9.7 pct, respectively. Figure 11(a) shows that a shear lip zone occurred and the fracture surface fluctuated greatly in steel L. In addition, the fracture surface consisted of a small cleavage facet, as shown in Figure 11(b). In contrast, Figure 11(c) shows that the fracture surface was relatively flat and little dimples were observed in steel H. This meant that there was less plastic deformation during the impact test. Moreover, a large river pattern extended to the surrounding area until it encountered the tear ridges in steel H, as shown in Figure 11(d), which indicated that more energy was

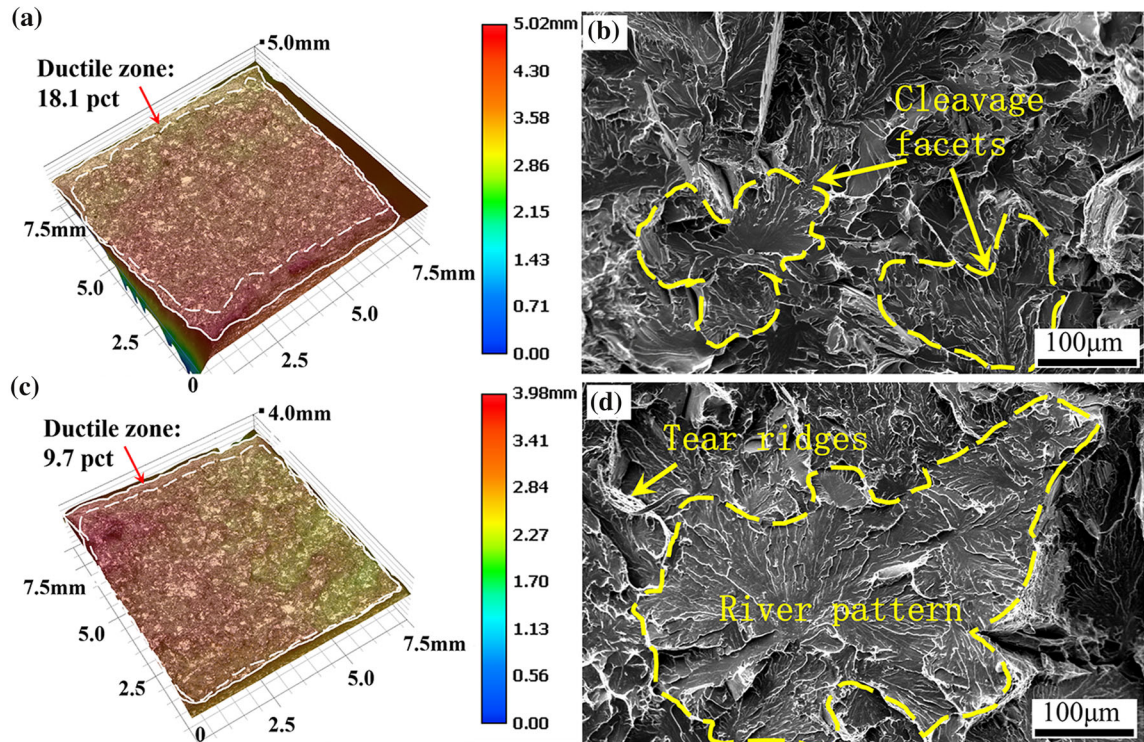


Fig. 11—Low-temperature impact fractures of (a) and (b) steel L and (c) and (d) steel H.

absorbed in steel L during the fracture process. To sum, steels with lower RE contents have higher low-temperature impact toughness under experimental conditions.

V. CONCLUSIONS

1. When the content of La was 0.010 wt pct in steel, the main inclusions in steel were La–O–S–Ti–Mg + MnS, the mean size of the inclusions was 1.3 μm , and the number of inclusions was 394.9 mm^{-2} . In steel with 0.068 wt pct La, the main composition of inclusions changed to La–O–P + La–P, the mean size of inclusions increased to 1.6 μm , and the number of inclusions increased to 665.9 mm^{-2} .
2. After the increase of La content, the area percent of AF decreased from 62.9 to 36.9 pct, the percentage of effective inclusions decreased from 78.6 to 41.6 pct, and the mean number of AF laths decreased from 2.9 to 2.3.
3. The most effective inclusion to induce the nucleation of AF in low La steel was the inclusion composited by La–O–S–Ti–Mg and MnS, whereas the most effective inclusion in high La steel was La–O–P + TiN. The percentage of effective inclusion in La–O–S–Ti–Mg + MnS was 86.8 pct, while that in La–O–P + TiN was 69.7 pct.

4. The mechanism of RE inclusions to induce the nucleation of AF may be the joint effect of the mismatch degree and the Mn depletion zone in steel.

ACKNOWLEDGMENTS

This work was supported by the National Natural Science Foundation of China (NSFC) under Grant Nos. 51804229 and 52074199.

CONFLICT OF INTEREST

On behalf of all authors, the corresponding author states that there is no conflict of interest.

REFERENCES

1. D.S. Sarma, A.V. Karasev, and P.G. Jönsson: *ISIJ Int.*, 2009, vol. 49, pp. 1063–74.
2. H. Nako, Y. Okazaki, and J.G. Speer: *ISIJ Int.*, 2015, vol. 55, pp. 250–56.
3. Q. Huang, X.H. Wang, M. Jiang, Z.Y. Hu, and C.W. Yang: *Steel Res. Int.*, 2016, vol. 87, pp. 445–55.
4. Y. Liu, G.Q. Li, X.L. Wan, H.H. Wang, K.M. Wu, and R.D.K. Misra: *Mater. Sci. Technol.*, 2017, vol. 33, pp. 1750–64.

5. C. Wang, J.J. Hao, J. Kang, G. Yuan, R.D.K. Misra, and G.D. Wang: *Metall. Mater. Trans. A*, 2021, vol. 52A, pp. 3191–97.
6. Y.X. Cao, X.L. Wan, F. Zhou, H.Y. Dong, K.M. Wu, and G.Q. Li: *Metall. Res. Technol.*, 2021, vol. 118, pp. 1–11.
7. J.S. Byun, J.H. Shim, Y.W. Cho, and D.N. Lee: *Acta Mater.*, 2003, vol. 51, pp. 1593–1606.
8. J.H. Shim, Y.J. Oh, J.Y. Suh, Y.W. Cho, J.D. Shim, J.S. Byun, and D.N. Lee: *Acta Mater.*, 2001, vol. 49, pp. 2115–22.
9. M.M. Song, B. Song, S.H. Zhang, Z.L. Xue, Z.B. Yang, and R.S. Xu: *ISIJ Int.*, 2017, vol. 57, pp. 1261–67.
10. T.K. Lee, H.J. Kim, B.Y. Kang, and S.K. Hwang: *ISIJ Int.*, 2000, vol. 40, pp. 1260–68.
11. B. Kim, S. Uhm, C. Lee, J. Lee, and Y. An: *J. Eng. Mater. Technol.*, 2005, vol. 127, pp. 204–13.
12. Y. Kang, S. Jeong, J.H. Kang, and C. Lee: *Metall. Mater. Trans. A*, 2016, vol. 47A, pp. 2842–54.
13. M.A. Van Ende, M.X. Guo, R. Dekkers, M. Burty, J. Van Dyck, P.T. Jones, B. Blanpain, and P. Wollants: *ISIJ Int.*, 2009, vol. 49, pp. 1133–40.
14. L.Z. Wang, S.F. Yang, J.S. Li, S. Zhang, and J.T. Ju: *Metall. Mater. Trans. B*, 2017, vol. 48B, pp. 805–18.
15. M.M. Song, C.L. Hu, B. Song, H.Y. Zhu, Z.L. Xue, and R.S. Xu: *Steel Res. Int.*, 2018, vol. 89, p. 1700355.
16. Z. Yu and C.J. Liu: *Metall. Mater. Trans. B*, 2019, vol. 50B, pp. 772–81.
17. Z.H. Wu, W. Zheng, G.Q. Li, H. Matsuura, and F. Tsukihashi: *Metall. Mater. Trans. B*, 2015, vol. 46B, pp. 1226–41.
18. R. Geng, J. Li, C.B. Shi, J.G. Zhi, and B. Lu: *Metall. Res. Technol.*, 2020, vol. 117, pp. 616–23.
19. S. Luo, Z.S. Shen, Z.M. Yu, W.L. Wang, and M.Y. Zhu: *Steel Res. Int.*, 2021, vol. 92, p. 2000394.
20. W.B. Xin, B. Song, M.M. Song, and G.Y. Song: *Steel Res. Int.*, 2015, vol. 86, pp. 1430–38.
21. C.S. Liu and B. Weblert: *Metall. Res. Technol.*, 2020, vol. 117, pp. 408–18.
22. Z. Liu, B. Song, Z.B. Yang, X.K. Cui, L.F. Li, L. Wang, and Z.R. Song: *Metals*, 2020, vol. 10, pp. 863–75.
23. X.K. Cui, B. Song, Z.B. Yang, Z. Liu, L.F. Li, and L. Wang: *Steel Res. Int.*, 2020, vol. 91, p. 1900563.
24. Y.M. Xie, M.M. Song, B. Wang, H.Y. Zhu, Z.L. Xue, A. Mayerhofer, S.K. Michelic, C. Bernhard, and J.L. Schenk: *Metall. Mater. Trans. B*, 2021, vol. 52B, pp. 2101–10.
25. R.A. Ricks, P.R. Howell, and G.S. Barritte: *J. Mater. Sci.*, 1982, vol. 17, pp. 732–40.
26. B.L. Bramfitt: *Metall. Trans.*, 1970, vol. 1, pp. 1987–95.
27. S.H. Zhang, N. Hattori, M. Enomoto, and T. Tarui: *ISIJ Int.*, 1996, vol. 36, pp. 1301–9.
28. Y. Kang, K. Han, J.H. Park, and C. Lee: *Metall. Mater. Trans. A*, 2014, vol. 45A, pp. 4753–57.
29. W. Gong, C. Wang, P.F. Wang, Z.H. Jiang, R. Wang, and H.B. Li: *J. Iron Steel Res. Int.*, 2021, <https://doi.org/10.1007/s42243-021-00579-1>.
30. K. Yamamoto, T. Hasegawa, and J.I. Takamura: *ISIJ Int.*, 1996, vol. 36, pp. 80–6.
31. H. Mabuchi, R. Uemori, and M. Fujioka: *ISIJ Int.*, 1996, vol. 36, pp. 1406–12.
32. Y. Tomita, N. Saito, T. Tsuzuki, Y. Tokunaga, and K. Okamoto: *ISIJ Int.*, 1994, vol. 34, pp. 829–35.

Publisher's Note Springer Nature remains neutral with regard to jurisdictional claims in published maps and institutional affiliations.